WIND ENERGY
Wind Energ. (2012)
Published online in Wiley Online Library (wileyonlinelibrary.com). DOI: 10.1002/we.535

RESEARCH ARTICLE

Wind turbine performance in shear flow and in the wake of another turbine through high fidelity numerical simulations with moving mesh technique

Joseph Seydel and Alberto Aliseda

Department of Mechanical Engineering, University of Washington, Seattle, Washington, 98195-2600, USA

ABSTRACT

We present numerical simulations of two horizontal axis wind turbines, one operating under the wake of the other, under an incoming sheared velocity profile. We use a moving mesh technique to represent the rotation of the turbine blades and solve the unsteady Reynolds averaged Navier–Stokes equations with a shear stress transport $k-\omega$ turbulence model. Temporal evolution of the lift and drag coefficients of the front turbine show a phase shift in the periodic cycle due to the non-uniform incoming free stream velocity. Comparisons of the lift and drag coefficients for the back turbine with the unperturbed behaviour of the front demonstrate the complex non-linear interactions of the blades with the wake, with a significant decrease in overall performance and two peaks at specific points in the cycle associated with local angle of attack modification in the wake. The vorticity field in the near wake shows tilting of the vortex lines in the wake due to the shear and a faster diffusion of the tip vortical signature compared with the uniform free stream velocity case. Observations of the wake–wake interaction show good agreement with recent studies that use different methodologies. Copyright © 2012 John Wiley & Sons, Ltd.

KEYWORDS
wind energy; turbulent wake; turbine–wake interaction; shear flow

Correspondence
Alberto Aliseda, Department of Mechanical Engineering, University of Washington, 4000 15th Ave NE Box 352600, Seattle, Washington 98195-2600, USA.
E-mail: aaliseda@u.washington.edu

Received 11 November 2010; Revised 8 September 2011; Accepted 15 September 2011

1. INTRODUCTION

As energy consumption increases and non-renewable energy sources are depleted, the need for clean renewable energy sources is continually increasing. Solar, wind, wave and tidal energy are all renewable sources that can contribute to the overall reduction in dependence on non-renewable fossil fuels. Wind energy has emerged as one of the leading technologies in providing cost-effective non-polluting renewable energy. However, wind power is still relatively expensive compared with non-renewable sources such as coal, despite reducing the cost per kWh by a factor of 10 over the past 20 years. Moreover, the widespread deployment of wind turbine farms is leading to an exhaustion of the prime sites, especially in small, highly technologically advanced countries in Western Europe. To further reduce the cost of wind energy and improve its availability as a non-polluting energy source, improvements in wind farm site optimization are necessary. Further understanding of the interactions between wind turbines and wakes from turbines located upwind from them is key to improving the utilization of the wind resource and raising the efficiency of installed turbines. In the last 30 years of rapid development, turbine designers have improved energy output by reaching higher into the atmospheric boundary layer and capturing more consistent and higher speed winds. With the increased height has come increased weight. If blade design is scaled up to maintain stiffness, blade weight increases with the blade length cubed, whereas the energy capture increases with the blade length squared.[1] To make wind turbines that are economically viable, weight reductions are required. The drawback arises from the combination of increased span and decreased weight resulting in turbines that are more dynamically active than their predecessors. The dynamic response of operating wind turbines to inflow turbulence can lead to structural fatigue and, ultimately, to failure. Inlet flow turbulence in wind turbines is most commonly generated by atmospheric phenomena

and wake-induced turbulence. As turbines become larger, the increased heights expose them to high-energy atmospheric phenomena such as low level jets.[2] These low level jets can cause shear velocity profiles that current wind turbine analysis methods are ill equipped to handle. Numerical simulations can provide the detailed flow physics with sufficient temporal and spatial resolution to understand the optimization of turbine design and operation with respect to the three key open questions described above: turbine–wake interaction, detailed aerodynamic loading on turbine blades and turbine operation in a sheared velocity profile. We present results from highly resolved numerical simulations of rotating turbines, using the sliding mesh model to address these issues. Conventional wind turbine design codes have traditionally relied on the blade element method (BEM) for their wake predictions. The BEM has been tremendously useful in wind energy design, but this method has its limitations. The BEM formulation begins to break down in unsteady flows and can be difficult to implement when temporal variations or non-axisymmetric velocities are present.[3] In the real world, however, temporal variations and non-axisymmetric flows are the norm rather than an exception.[4] Errors in the flow analysis, caused by these variations, can cause errors in the loading analysis resulting in premature failure of the rotor. Most computational fluid dynamics (CFD) analysis that has been performed to date assumes a uniform inflow condition that, as explained above, is an idealized condition, not fully representative of the real world. Work has recently begun on using CFD to simulate rotors in non-uniform flows.[5–7] In this paper, two turbines, one partially immersed in the wake of the other, operating in a shear flow were modeled using a sliding mesh approach. In Section 2, we describe the methodology and the boundary conditions used in our simulations. In Section 3, we present comparisons of the results from the simulation to experiments, validating the methodology used for this study. In Section 4, we first analyze the results from the front turbine to address the influence of the sheared velocity profile on its performance. The results from the second turbine, located in the wake of the first one, are then analyzed and compared with the first, unimpeded turbine, in order to understand wake–turbine interaction issues. In Section 5, we summarize our conclusions from the analysis and point to implications on efficient turbine spacing rules and aerodynamic loading prediction.

2. NUMERICAL MODEL SETUP AND BOUNDARY CONDITIONS

CFD is been increasingly used to improve the overall understanding of the flow physics of wind turbines. A full three-dimensional (3D) analysis of turbine and wake can eliminate some of the limiting assumptions that are made with other methods such as blade element or lifting line methods. Numerical investigations of wind turbine blades and/or the resulting wake can be performed using numerous combinations of approaches and turbulence models. We use the Reynolds averaged Navier–Stokes equations, with a turbulence model to provide closure for the Reynolds stress term and the sliding mesh model to simulate the flow around the rotating turbine blades.

2.1. Turbulence model

The Reynolds average Navier–Stokes equations describe the mean fluid variables in a turbulent flow.[8] Briefly, Reynolds averaging starts by decomposing the velocity, U(x, t) (and all other fluid variables such as pressure), into its mean value, $\overline{U(x,t)}$, and its fluctuation, $u'(x,t)$. The resulting equation has the same form as the Navier–Stokes equations with the addition of the Reynolds stress term. This terms needs to be modeled as a function of other conserved or transported variables to provide closure. Of the many turbulence models available, we use the shear stress transport (SST) model, developed by Menter,[9] which has been showed to solve the limitation of the κ–ω model, whereas the boundary layer solution depends strongly on the freestream value of ω. The SST κ–ω model is identical to the κ–ω model for the inner half of the boundary layer but transitions to a κ–ϵ model for the freestream. The production term is limited in the SST model to prevent the build-up of turbulent kinetic energy in stagnation regions and is given by

$$P_k = \mu_T \frac{\partial u_i}{\partial x_j}\left(\frac{\partial u_i}{\partial x_j} + \frac{\partial u_j}{\partial x_i}\right) \Rightarrow \tilde{P_k} = \min(P_k, 10\beta^* \rho\kappa\omega) \tag{1}$$

where μ_T is the turbulent, or eddy, viscosity; $\partial u_i/\partial x_j$ are the different elements of the velocity gradient tensor; β^* is a numerical coefficient (=9/100); ρ is the fluid density; κ is the turbulent kinetic energy; and ω is the specific dissipation.

2.2. Numerical solver

The numerical simulations were performed in Fluent 6.3 (ANSYS Inc., Cannonsburg, PA.). A sliding mesh approach was used to capture the dynamics of the unsteady flow field around the turbines, including the realistic boundary conditions involved in the sheared velocity profile at the inlet, the off-axis location of the turbines and the non-axisymmetric simulation domain. In the sliding mesh approach, multiple cell zones are created and bound through interface zones. Adjacent cell zones are coupled through a grid interface, along which the motion of the cell zones will occur. Because the cell zones are moving with relationship to each other, the face grid of the interface zones will not be aligned at each time step. This

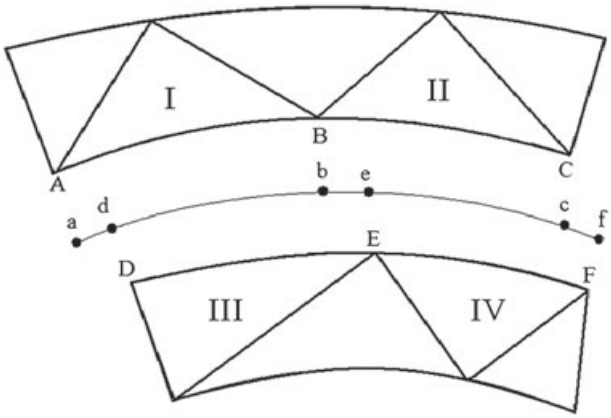

Figure 1. Schematic of the non-conformal interface. Points A–D, B–E and F–C are coincident at the beginning of the time step but become distinct because of the rotation of the upper volume with respect to the lower one, which makes A move to a, B move to b, and C move to c.

misalignment requires the flux across the interface to be calculated using a non-conformal interface at each time step. In the example shown in Figure 1, the interface zones are defined by faces A–B, B–C, and D–E, E–F. The intersection of these faces creates faces a–d, d–b, b–e, etc., which become the interior face that couples the two fluid zones. To calculate the flux into zone III, we used faces d–b and b–e whereas we ignored A–B and D–E. The interface between the two fluid zones is recalculated after each time step, and the process is repeated. All convective terms are calculated using a second-order upwind scheme. For second-order accuracy of an unstructured grid, Fluent uses a multidimensional linear reconstruction approach, as described by Barth and Jefferson.[10] This approach uses a Taylor series expansion of the cell centered value about the cell centroid. For this analysis, the SIMPLE algorithm was used to iterate the pressure field. Using this algorithm, it is not necessary to fully resolve the pressure–velocity coupling between each consecutive step. This method starts by calculating an approximate velocity and pressure gradients and solving the discretized momentum equation based on the boundary conditions. A pressure correction term is then computed at each cell, and the velocity field is updated to satisfy the continuity equation. To iterate, the algorithm uses under-relaxation factors to update to a new pressure and velocity field.

2.3. Solid wall modeling

The wall contributes a considerable portion of the mean vorticity and turbulence to the flow. Because of this, near-wall modeling must be handled carefully. There are two approaches to modeling near-wall flows. The first approach modifies the turbulence models and requires a mesh that can resolve the flow all the way through the viscous sub-layer. The second approach does not attempt to capture the flow all the way to the wall but uses semi-empirical models, or wall functions, to bridge the gap between the outer layer and wall. The wall function used corresponds to an approximation of the mean velocity near the wall $U^* = 1/\kappa \ \ln(Ey^*)$, where U^* is defined as $U^* = UC_\mu^{1/4}k^{1/2}\rho/\tau_w$ and $y^* = yC_\mu^{1/4}k^{1/2}\rho/\mu$. μ is the dynamic viscosity, ρ is the density, k is the turbulence intensity, τ_w is the wall shear stress, and E and κ are empirical constants equal to 9.793 and 0.4187 (von Karman constant), respectively. This approach can save significantly on computational resources and eliminates the need to modify the turbulence model to account for the wall. The wall function approach assumes that the flow follows the logarithmic law-of-the-wall near the wall. This assumption can cause the wall function to break down for low Reynolds numbers flows or in the presence of strong pressure gradients. In wind turbine applications, this can be an issue. For large angle of attacks, where the pressure peak at the leading edge is exacerbated and separation occurs immediately on the suction side, this can cause difficulty in maintaining the recommended y^+ at the wall. Simulations presented here were conducted under conditions ensuring the flow remained attached except in a very small region near the blade root.

2.4. Turbine geometry: NREL Phase VI rotor

The National Renewable Energy Laboratory (NREL, Golden, CO.) Phase VI rotor was used for this study. The availability of the test data on this geometry from the NASA Ames 80 × 120 ft wind tunnel (NASA Ames Research Center, Moffet Field, CA.)[11] made this the ideal geometry to perform this study. This is a stall-regulated, two-bladed turbine, with 5.53 m radius and hub height of 12.2 m. We reproduce in our simulations the operating conditions at 7 m s^{-1} free stream velocity,

Figure 2. NREL Phase VI rotor in operation during wind tunnel test (from Hand *et al.*[11]).

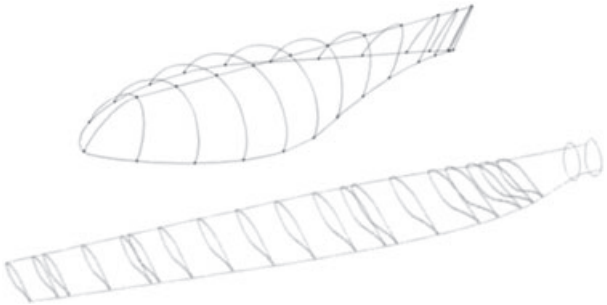

Figure 3. NREL Phase VI wireframe. The geometry created for the tip of the blade is shown in the top.

with an ambient turbulence intensity of 2% and a rotational speed for the blades of 72 rpm. The key non-dimensional parameters are the tip speed ratio, $\Lambda = 5.41$, and the Reynolds number, $Re_R = 2.2\ 10^6$ (Figure 2).

A 3D model of the baseline NREL Phase VI rotor blade was constructed using the 3D modeling capability of Gambit 2.4.6. The blade itself is composed of a series of S809 airfoils from root to tip, which are tapered and twisted to achieve the desired performance. The blade cross sections are defined using NREL tabulated data of the taper and twist at various radial distances. From the tabular data, wireframes of the blade and root were created, and surfaces were constructed using Gambit's net surface creation.

Because actual dimensions of the blade tip were not available, a wireframe was constructed using measurements from NREL documents for reference, shown in Figure 3. The base of the blade tip wireframe starts at the $0.96R$ blade section (where R is the blade radius). This cross section was offset by $0.001R$, and a series of nodes was placed along the edges. Using this offset as the starting point ensures that the curves are tangent to the blade surface along the face. These nodes were then projected onto the tip base and top edge, which was defined as the camber line of the airfoil at $r/R = 1$. Using these nodes as control points, non-uniform rational B-spline (NURB) curves were used to ensure that the blade tip would be tangent to the blade at the transition. The dimensions of the curvature at the leading edge were based on the planform view of the blade. An arc, with a radius of $0.0038R$, was swept from the tip of the base to the camber line to create the leading edge. The NURB curves were then clipped at the $0.96R$ blade section, and a net surface was again used to create a smooth face.

To simplify the creation of prism layers, we rounded the trailing edge. The sharp angles at the edge of the actual geometry create skewness issues in the numerical grid, which are difficult to resolve. The rounding of the edge shortened the chord length by 0.4%. This process can be observed in Figure 4. A numerical study conducted by Do[12] demonstrated that clipping an airfoil at this chord position does not affect any of its aerodynamic characteristics, including its shedding frequency, which is the most sensitive to trailing edge modifications.

The turbine hub geometry was included in the model to create domain closure at the centerline and to contribute centerline vorticity present in the actual flow. The hub used is not representative of actual NREL wind turbine hub geometry, but is believed to be an improvement over other methods that omit the hub completely. Details on the hub, one of the blades, and blade tip are shown in Figure 5.

For the sliding mesh model, the rotating sub-domain must be defined inside the fluid volume. This sub-domain rotates about the turbine axis and must be axisymmetric about the axis of rotation. The sub-domain used in the analysis is a cylinder

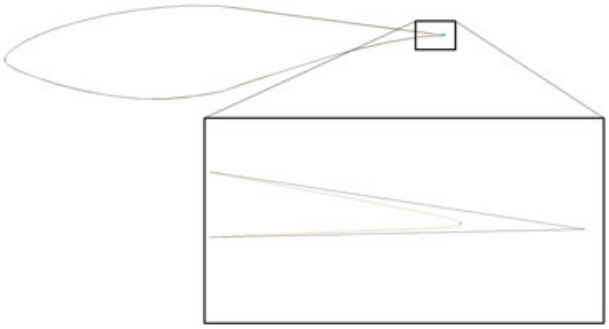

Figure 4. Rounding of the trailing edge of the blade section to avoid skewed grid elements.

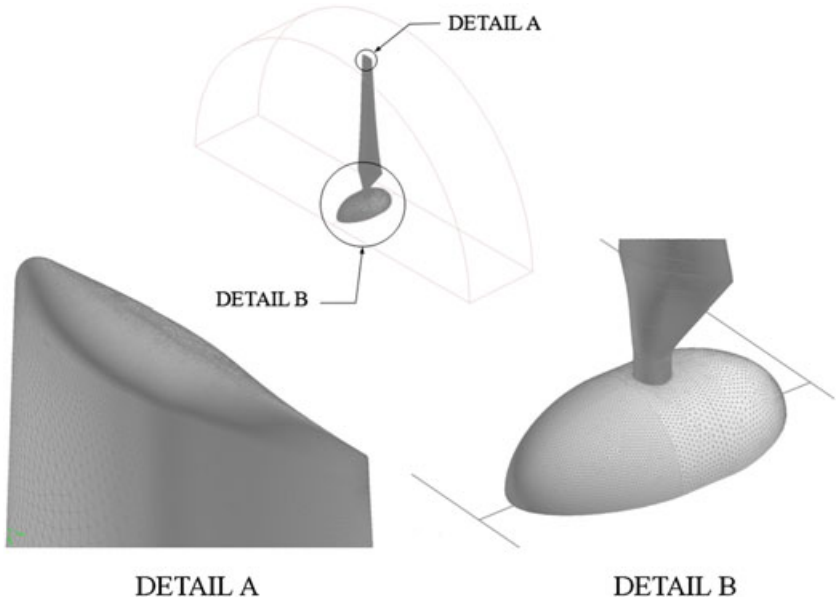

Figure 5. Blade tip and hub shown with moving sub-domain boundary.

with a radius of $1.1R$ and length of $0.5R$. The overall domain is shown in Figure 6, where we can appreciate the two disks with the moving meshes around each of the two turbines, as well as the separation between the turbines: $1R$ lateral offset and $2R$ downstream spacing. An unstructured mesh was applied at the blade surface. With the use of a fully unstructured mesh, it is possible to concentrate grid points in the area of interest and to use growth functions to limit quality issues away from these areas. These growth functions also become crucial when transitioning from the blade to the interface. For sliding mesh models, the interface between the sub-domain and the rest of the flow field must have similarly sized face grids. Numerical errors arise when there is a discontinuity in grid size at the interface. A fine numerical grid is required at the blade tips and edges to ensure sufficient resolution in the regions of highest curvature and largest pressure gradients. A model using a fully structured grid would need a high mesh density in the entire moving sub-domain to adequately capture the blade tips and satisfy the requirement that the interface be nearly uniform. If the entire flow field is also to be structured, then this small grid size would propagate in all directions, which would ultimately produce a grid size that is unmanageable. The first cell height of the prism layer was set equal to 0.002 m to ensure that y^+ was between 30 and 300 at the edges of the blade.

When using an unstructured grid, it is important to recognize the potential for additional numerical diffusion caused by the limited spatial resolution. To address this additional numerical diffusion, a technique of manual wake clustering was used to concentrate elements in the flow field downstream of the turbine. A cylindrical surface with a radius of $1.02R$ and a length of $8R$ was created in the flow domain, starting at the domain interface. This surface was then meshed and used as the source for a growth function. The initial size of the elements is $0.04R$. A cross sectional view of the mesh on a plane that cuts through the hubs of both turbines is shown in Figure 7. The apparent skewness of grid elements is an artifact of a

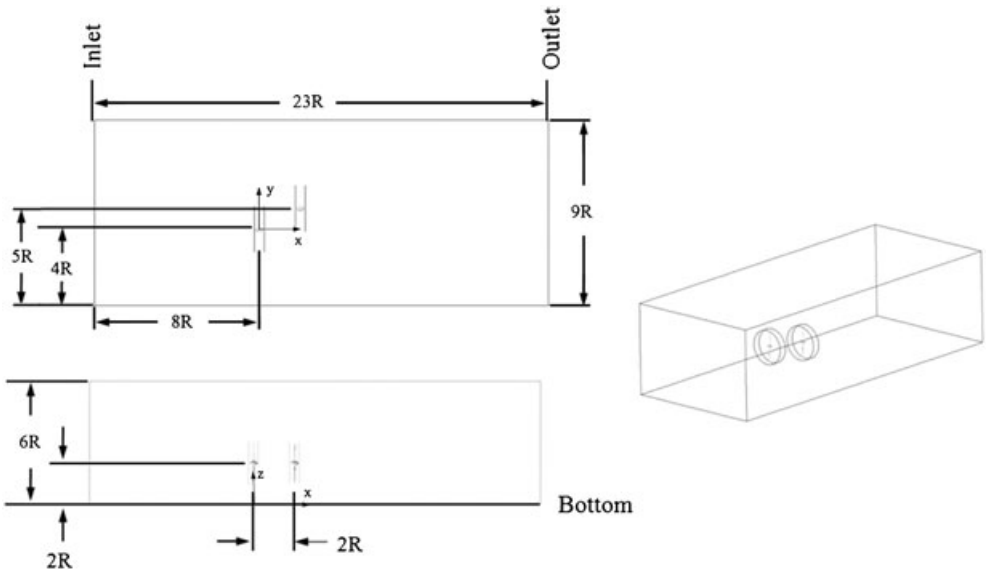

Figure 6. Two-rotor external flow domain.

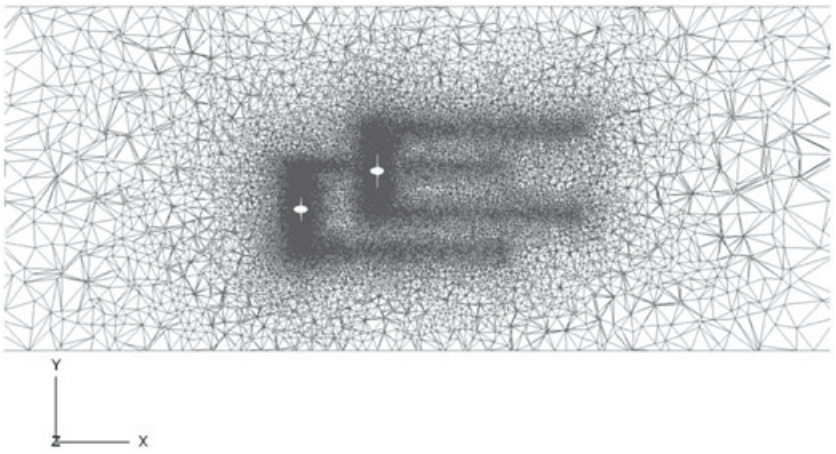

Figure 7. Manual clustering of the mesh to minimize dissipation in the wake.

cross-section slicing through the unstructured 3D grid and does not represent actual element skewness. This technique was used on both upstream and downstream turbines with the same parameters. The total grid count for the two-rotor model is 17 10^6 cells.

2.5. Boundary conditions

A shear velocity profile was specified at the inlet and sides of the fluid region. This profile is defined by a linear increase in velocity from 0.1 m s^{-1} at the bottom of the domain to 7 m s^{-1} at the hub and a constant velocity of 7 m s^{-1} above that. The rotor is given a rotational speed of 72 rpm, which results in a tip speed ratio of 5.41. This profile was used to allow for comparison with the NREL Phase VI test data at the top of rotation and to create a strong shear profile for the bottom half of the rotation. The turbulence intensity at the inlet was set to 2%. The top, sides and bottom surfaces were set to constant velocities, equal to the velocity in the inlet profile corresponding to the vertical coordinate. This way, the velocity is kept constant at the boundaries far away from the turbines, although it evolves inside the domain because of the presence of the turbines and their wakes. The velocity normal to the walls was set to zero. The use of a wall boundary along the bottom would allow the growth of a bottom boundary layer, but would make the velocity a variable as a function of distance

downstream, thereby making comparisons between the two turbines inadequate. The outlet is set as a pressure outlet with a backflow turbulence intensity of 2%. A time step of 0.002315 s (1° rotor rotation per time step), with 20 sub-iterations per time step, was used for the transient simulation. This time step is below the shedding frequency of the tested NREL Phase VI blade[13] and gives reasonable accuracy without excessive computational expense. Zhale and Sørensen[14] showed that the difference in computed torque between a time step of 0.002 and 0.001 s was around 2%, providing marginal improvement at greatly increased cost. With this time step and 20 sub-iterations, the residuals drop by three orders of magnitude at each step. To initialize the flow field, we used a time step of 0.02315 s with 20 sub-iterations. This large time step allowed for information from the solution initialization to wash out of the computational domain before iterating at the regular step size. A total of 20 revolutions was used to initialize the flow field, but fewer could be used if the field is monitored regularly. Monitoring can be performed by plotting the area-weighted value of a chosen flow variable for a cut plane near the outlet of the domain. The solution can be considered to be steady once the variable changes by less than 5% from one rotation to the next. After the initial 20 revolutions were completed, an additional 2.5 revolutions were run using the smaller time step. We checked for convergence not only of the integral forces but also of the local lift and drag coefficients at different sections of the blade. Starting approximately after 1.5 revolutions, we did not find any variations in the values with the ones calculated for a time one revolution earlier, beyond the small-scale fluctuations associated with the turbulent character of the flow. This was the criterion for stopping the simulation. This is consistent with Figure 3 from Zahle and Sørensen,[14] which shows the almost instantaneous convergence of the flow for the small time step. Running the simulation for such a long time at this small time step (with the significant computational cost associated with it) allowed us to ensure sufficient time for the shed vortices in the wake to be convected past the downstream turbine in the two-rotor simulation.

3. COMPARISON WITH EXPERIMENTS AND VALIDATION OF THE NUMERICAL METHODOLOGY

3.1. Validation of the numerical methodology: comparison of the single turbine simulation in uniform flow velocity

We used the results of the simulation of flow around a single turbine in uniform flow, performed under the same methodology as the two-turbine simulation, to compare against similar experimental and computational results. This is a first step in the validation of our results, ensuring that our methodology captures the physics of the simpler case.

A contour plot of the non-dimensional centerline velocity, Vx/V is shown in Figure 8. The velocity profile of the wake shows that the transition to a self-similar wake occurs around 4–5 radii downstream of the turbine, which is in agreement with test data.[15]

The results from our simulation were also compared with Duque's[16] work performed on the NREL Phase VI rotor in a uniform flow. The sliding mesh approach shows good agreement with Duque's results in pressure coefficient and velocity. Comparison of the velocity contours along the blade between our simulation and the 7 m s^{-1} case from Duque *et al.*[16] is shown in Figure 9. We can see identical features in the velocity results near the blade, tip and wake. The key differences seen near the blade root can be attributed to the addition of the hub in the current study.

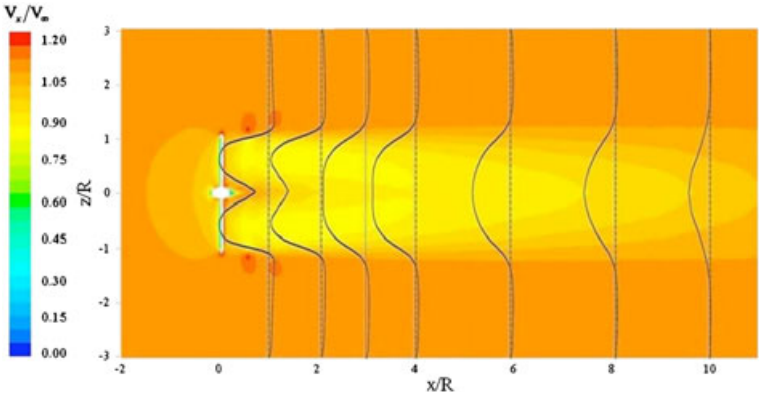

Figure 8. Centerline velocity profile for a single turbine (NREL PHASE VI geometry) in uniform flow from numerical simulation by using the sliding mesh method.

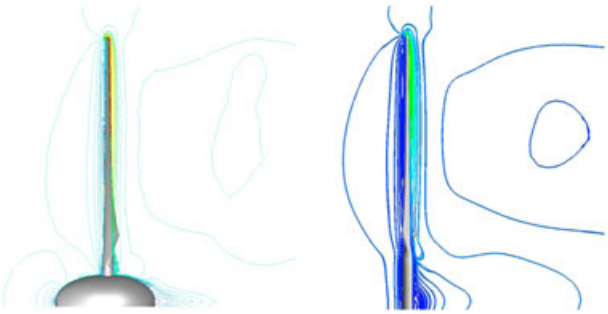

Figure 9. Velocity contours for current study (left) demonstrate similar patterns to those shown in Duque[16] (right).

3.2. Validation of the two-turbine simulation in sheared flow: comparison with experimental test results for NREL phase VI

To ensure the consistency of the results obtained from the simulation of two turbines in a sheared flow with the single turbine simulations, we compared several quantities obtained in a preliminary simulation of a single turbine in uniform flow with our simulation from the top blade on the front turbine, when the blades are passing through the vertical position and therefore the top blade is subject to an incoming uniform flow. The variables were almost identical. This validates that this simulation is converging and is still capturing the physics of this complex flow. To further validate the two-turbine simulation, we compare the pressure coefficient $C_p = -(P - P_\infty)/(0.5\rho(V_\infty^2 + (\Omega r)^2))$, at different sections of the front blade at the top position, against the experimental values reported from the NREL Phase VI rotor blades test.[17] The results of this comparison can be seen in Figure 10. We find very good agreement between the simulations and the experimental measurements, with the peak negative pressure near the leading edge of the suction side of the airfoils being the area were the simulation has trouble and consistently underpredicts the values of C_p. As the peak is less marked for the blade sections closer to the tip, $r/R - 0.8$ and 0.95, the accuracy of the numerical results is much better than for the mid-blade sections, where the suction peak is much more prevalent, $r/R = 0.3$ and $r/R = 0.47$. This is typical of any simulation of this type and has minimal impact on the integral quantities such as lift, torque and power. This limitation of the numerical technique is associated with the fact that the y^+ is at or below the recommended minimum for use of wall functions in the areas of the largest error. Improvements in y^+ could be made during grid refinement once a more accurate estimate of the local flow velocity has been established. The 3D flow field and curvature in these areas complicates setting a single first cell height. The first cell height was set to obtain a y^+ near 30 at the end of the blade to ensure the wall function calculated a more accurate solution of the tip vortices. The most accurate approach is achieved by modeling the near-wall region, but doing so increases the number of cells in the prism layer by a factor of 4,[18] making the node count unrealistic for this type of study.

4. RESULTS AND DISCUSSION: MULTIPLE ROTOR MODEL

In this section, we review the results from the simulation of two NREL Phase VI rotors in a tandem configuration where the second turbine is located two radii downstream of the front turbine and at one radius lateral offset from the axis of rotating, as shown in Figure 6. The free stream was modeled with a sheared velocity to make the results more relevant to realistic configurations and to take advantage of the modeling capabilities of the sliding mesh technique. The upstream turbine demonstrates a sinusoidal fluctuation of the lift and drag coefficients, defined in terms of the relative velocity $C_{l,d} = L, D/(1/2\rho c(V_\infty^2 + (\Omega r)^2)$, as a response to the passage of the blades through the shear profile. A phase shift in the drag coefficient for the upstream turbine is present, decreasing with radial position. This phase shift is consistent with the results reported by Sørensen[7] and Zahle[14]. In all plots, an azimuthal position of 0° corresponds to the blade in a vertical orientation (i.e. with the blade tip furthest from the bottom surface).

Figures 11 and 12 show the velocity contours in vertical and horizontal planes, respectively. We can see the structure of the wake, including the acceleration at the tip vortices and the detached flow behind the hub. It is interesting to note how the velocity field impinging on the second turbine depends strongly on the position of the upstream blade, for this close positioned turbines.

Figure 13 shows the evolution of the drag coefficient versus position of the blade. The decrease in drag coefficient phase shift as the radial distance is increased can be attributed to the influence of blade velocity on the relative velocity triangle for different sections of the blade. The change in relative velocity affects the angle of attack and results in fluctuations of the aerodynamic forces: tangential velocity increases with radial distance and becomes a larger component of the relative

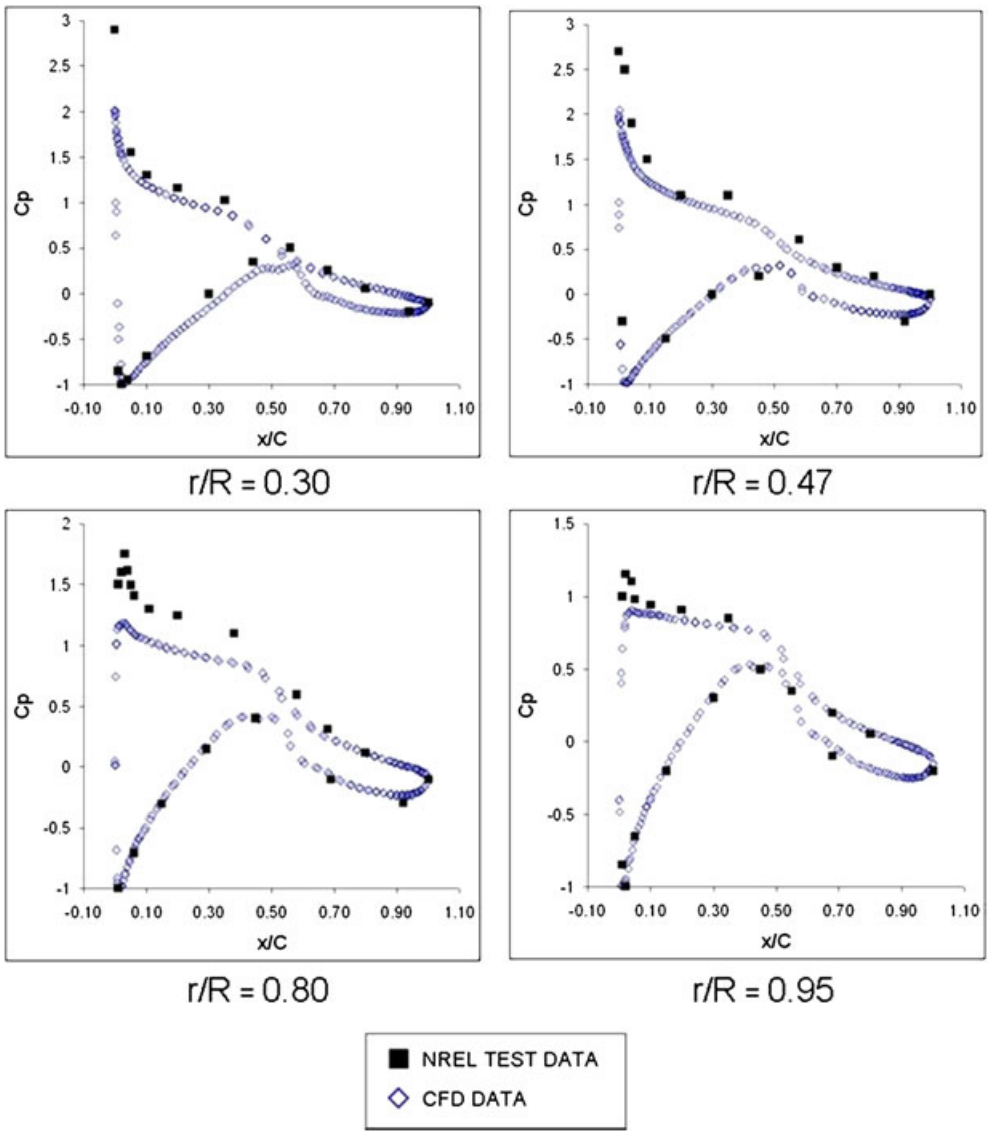

Figure 10. Plot of pressure coefficient at four radial distances along the blade showing the improvement of the solution near the blade tip.

velocity, therefore reducing the effective angle of attack. Because the incoming velocity is not uniform, particularly in the downstream turbine where the flow has an induced downwash around 90° and upwash at 270° due to the wake (and the sense of rotation) of the upstream turbine, the drag and lift coefficients present high-frequency fluctuations overlapped with the predominant harmonic at the frequency of rotation of the turbines.

A plot of the transient lift and drag coefficients of the second (downstream) turbine show a clear response to the wake of the upstream turbine. The relative inflow velocity decreases as the blades pass through the wake of the upstream turbine. The evolution of the lift coefficient, shown in Figure 14, is clearly non periodic, even for the upstream turbine. The lift remains almost flat from 0° to 90°, as the blade moves through the uniform velocity field, but it fluctuates between 90° and 270° because of the shear velocity profile in the case of the upstream turbine. For the downstream turbine, the behaviour is much richer because of the strong interaction with the wake of the upstream turbine. Drag increases noticeably in the fourth quarter (between 270° and 360°) as a result of the effect of the upstream wake on the incoming velocity and blade angle of attack. For the downstream turbine, the lift on the blade is reduced to its minimum value (about 0.2) for the entire region in which the blade is immersed in the wake of the upstream turbine (0° to 180°) but surges above the maximum value (approximately 0.9) as it leaves the wake and moves through the upper reaches of the sheared velocity profile. At

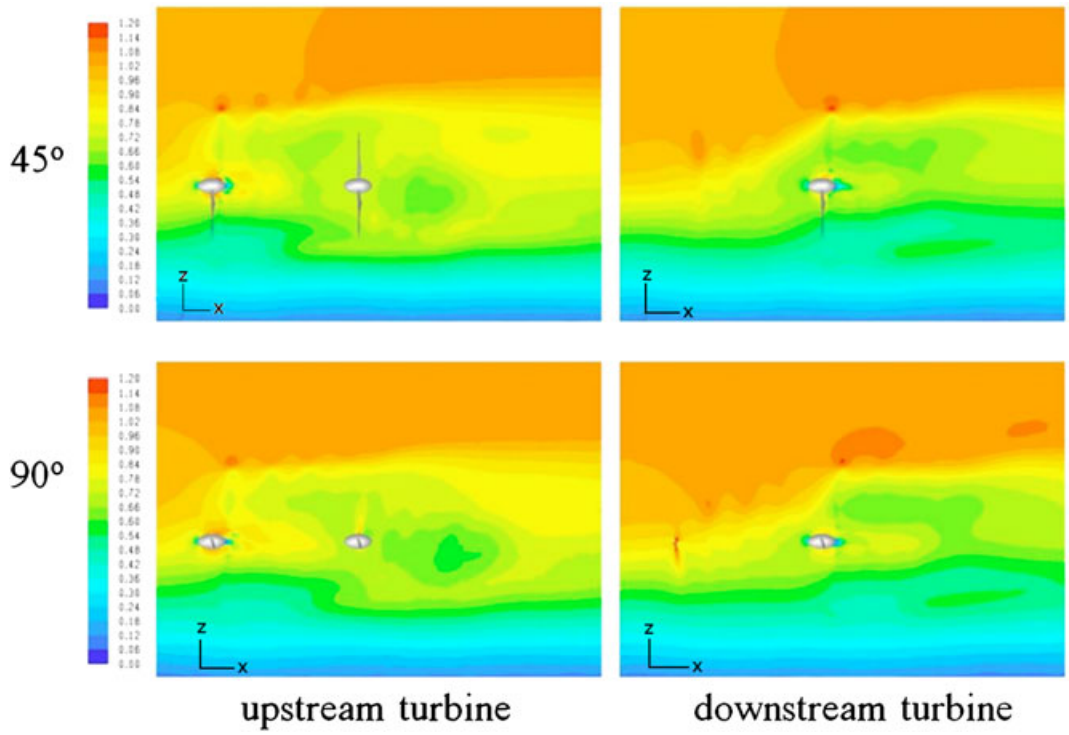

Figure 11. Contours of non-dimensional velocity in a horizontal (X–Y) plane at the turbines hub height. The blades are at 135° from the vertical.

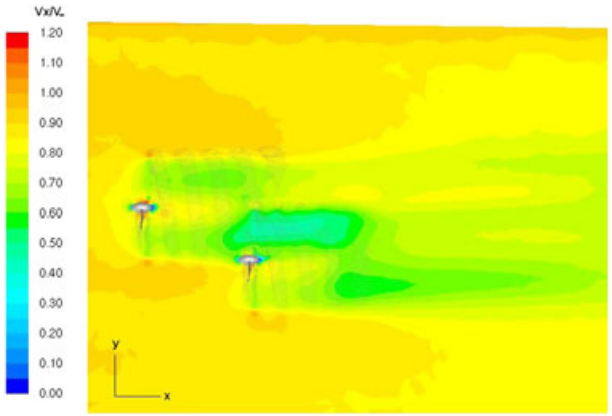

Figure 12. Contours of non-dimensional centerline velocity for two different vertical streamwise (X–Z) cross planes. On the left, the plane shown is along the upstream turbine axis, at $y = 0$ (the downstream turbine is shown just to outline its position, the hub is on a different plane). On the right, the plane shown is along the downstream turbine axis (at $y = -1R$). The flow is presented at two instants within the blade rotation cycle: the top subfigures show the flow when the blades are at 45° from the vertical, and the bottom subfigures are for the blades at 90° from the vertical.

about 315°, the lift coefficient peaks for every section of the blade because of the upstream turbine inducing a favorable incoming velocity in this quadrant. This is a result of the coupling between the turbine spacing, lateral offset and tip speed ratio, which are specific to this simulation, but the importance of this observation is that this physical effect will occur for all conditions, albeit at different positions in the cycle, leading to high loads and high-frequency harmonics. It then returns to the reference value at the vertical position (0°). A brief increase in lift and drag can also be seen at the point where the blade passes through the centerline of the upstream turbine (90°). This can be attributed to the small acceleration of the flow as it wraps around the hub of the upstream turbine and the separated region immediately behind it. Similarly, the reduced

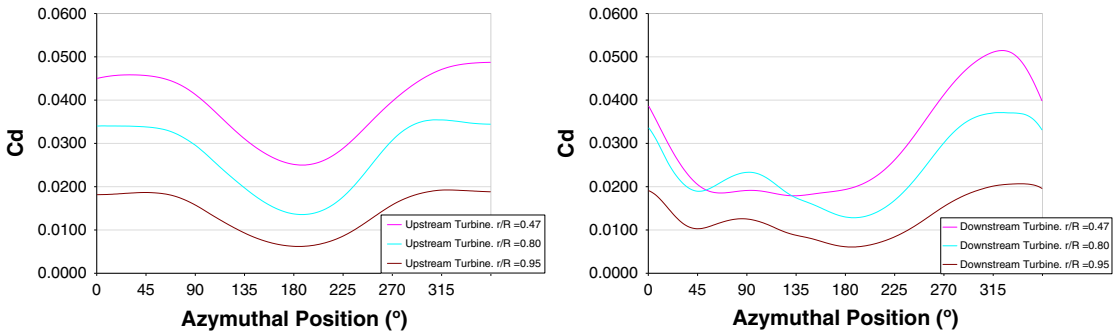

Figure 13. Drag coefficients versus position for upstream rotor (left) and downstream rotor (right).

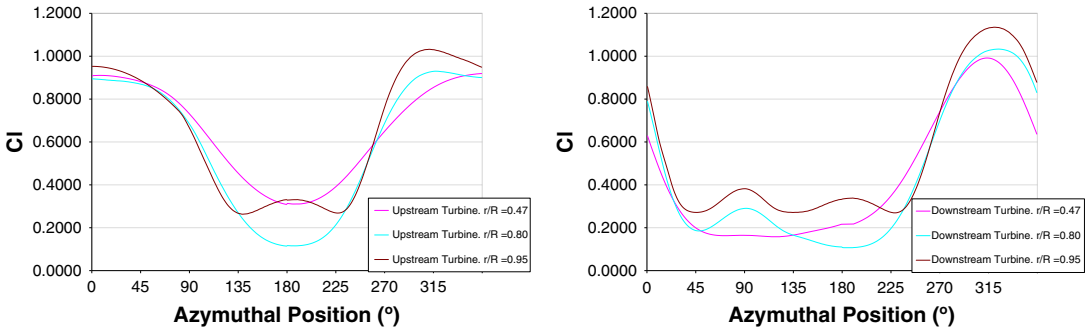

Figure 14. Lift coefficient versus position for upstream rotor (left) and downstream rotor (right).

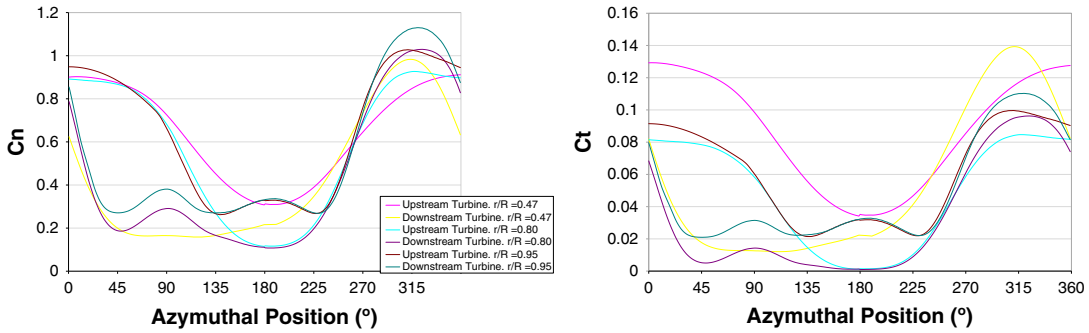

Figure 15. Normal (left) and tangential (right) force coefficients plotted versus position for both rotors.

loading of the cylindrical section of the blade at the root induces a low blockage and a resulting high relative speed in that area of the wake. Both of these contributions create a high local velocity coming from the upstream turbine that, in this configuration ($1R$ lateral spacing, $2R$ downstream spacing), is clearly still a coherent feature of the flow impinging on the downstream turbine. This feature can be seen in the contour plots of non-dimensional velocity in Figure 11. The velocity in these contour plots is made non-dimensional using the maximum freestream velocity of 7 m s^{-1}. Similar physics can be observed in Figures 13 and 15, where the drag, normal and tangential coefficients are plotted, respectively. The same high-frequency forcing on the blades can be observed, with the main feature to be highlighted is the large increase in the drag and tangential forces on the blade sections near the root, compared with the sections near the tip as a result of the high angle of attack found in those sections, resulting in very similar lift (and normal force) coefficients with much higher drag (and tangential force). An additional observation from Figure 15 is that the behaviour of the upstream and downstream turbines converge to a certain degree in the region where the downstream blade is further away from the wake of the upstream turbine, between 225° and 300°, diverging when they approach the vertical position where the downstream blade is exposed to the induced velocity from the upstream turbine. This region around 315° is where the lift coefficients for the downstream turbine peak.

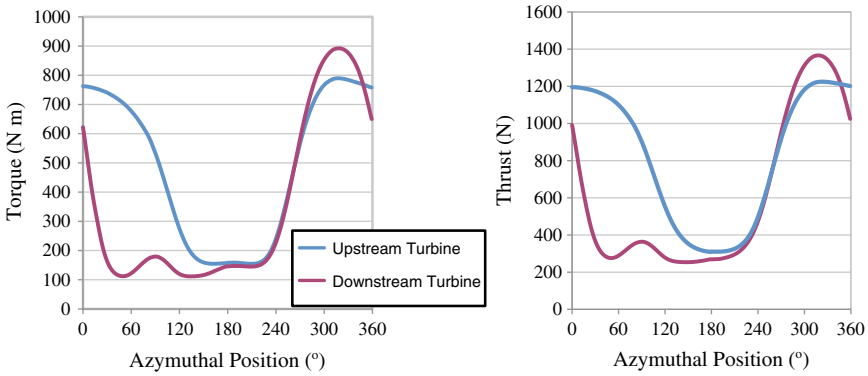

Figure 16. Torque (left) and thrust (right) for the two turbines, plotted versus the position of the blade with respect to the vertical axis.

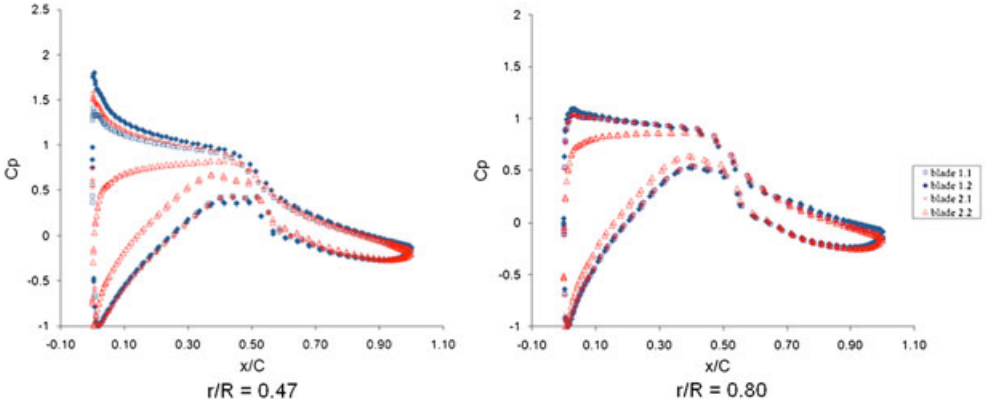

Figure 17. Comparison of the upstream and downstream pressure coefficients at two radial positions for blades in the horizontal position (azimuthal position = 90°). In the legend, blade N.M refers to blade M on turbine N. For example, 2.2 is blade 2 on the downstream turbine and the blade immersed in the wake of the upstream turbine.

The overall performance of the turbines is shown in Figure 16. The torque and thrust (overall drag force on the turbine) are plotted dimensionally for both turbines. These integral quantities follow a very similar trend as observed in Figure 15, as the behaviour for all sections of the blade is qualitatively the same. Although the values at the top of the cycle (0°) are consistent with the values from the literature for blades in uniform flow, specially for the upstream turbine, the drop off as the blade sinks into the sheared velocity profile (or the wake for the downstream turbine) highlights the influence of a non-uniform velocity profile on the turbine performance. The upstream turbine is relatively close to a sinusoidal variation. The downstream turbine, however, sees a very steep fall off as it enters the wake between 0° and 60°, stays low as it travels through the bottom of the sheared velocity profile (from 120° to 180°). Performance matches the upstream turbine in the low velocity region outside the wake (180–270°) and then peaks because of the interaction with the upstream turbine wake, at 315°, coming down with a steep slope as it approaches the vertical position.

Figure 17 shows the difference in C_p between all four blades while in a horizontal position (90°). At a radial distance of $r/R = 0.80$, the difference between the C_p of the blade in the wake, blade 2.2, and the other three blades is less than at a radial position of $r/R = 0.47$. When the blades are in the vertical position (0°), it can be seen in Figure 18 that the difference in pressure coefficient at a radial distance of $r/R = 0.80$ between the upstream and downstream turbine is small. The difference in pressure coefficients is somewhat more pronounced at a radial distance of $r/R = 0.47$. A comparison of these six plots provides information about the effect that local changes in inflow velocity have on aerodynamic forces on the blade.

The effect of the shear profile is apparent in the iso-surfaces of constant vorticity shown in Figure 19. These iso-surfaces illustrate the decreased lift due to the shear profile and the resultant skewing of the wake. The iso-surfaces for the blades at 45° in the rotation cycle, Figure 20, show a clear interaction of the downstream blade with the shed vortex from the upstream turbine. For the combination of angular velocity, turbine separation and inflow velocity profile modeled, the downstream turbine passes directly through the coherent vortices shed by the upstream turbine. Plots of the centerline velocity profiles

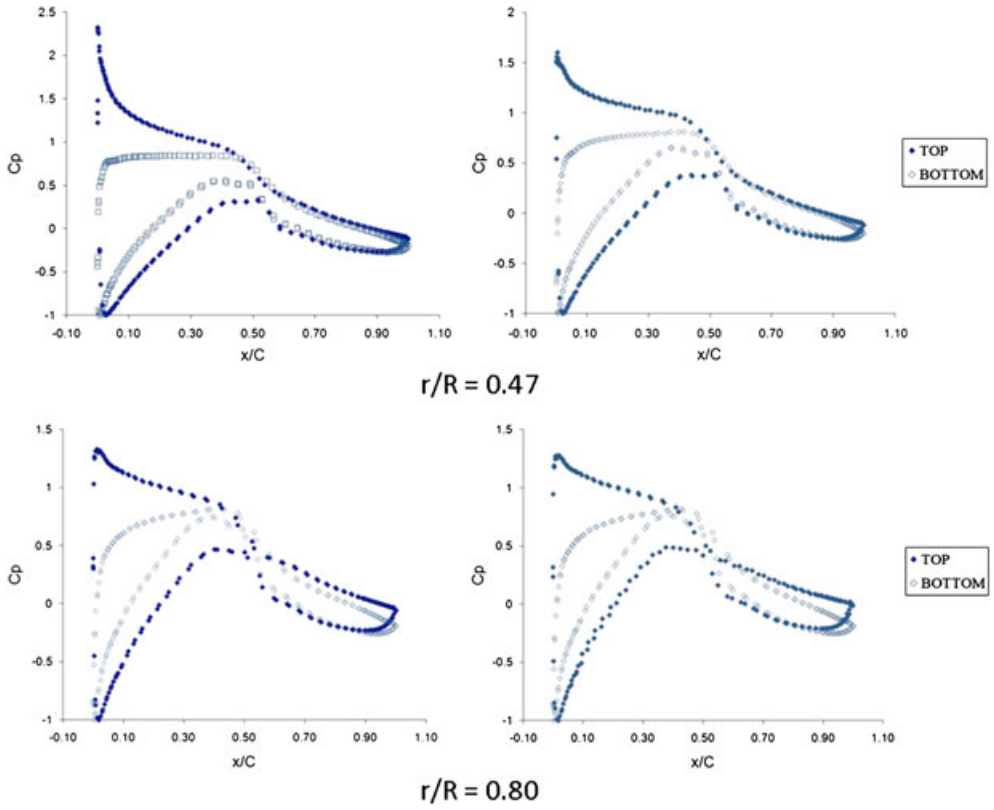

Figure 18. Pressure coefficients for the upstream (left) and downstream (right) turbine. In both cases, the blades are in the vertical position (azimuthal position = 0°). Symbols marked as TOP refer to the blade that is pointing upwards, at 0° with the vertical, and are therefore subject to a uniform flow, at least in the case of the upstream turbine. Symbols marked as BOTTOM refer to the blades pointing downwards, at 180° with the vertical, and are therefore subject to a pure shear velocity profile, at least in the case of the upstream turbine.

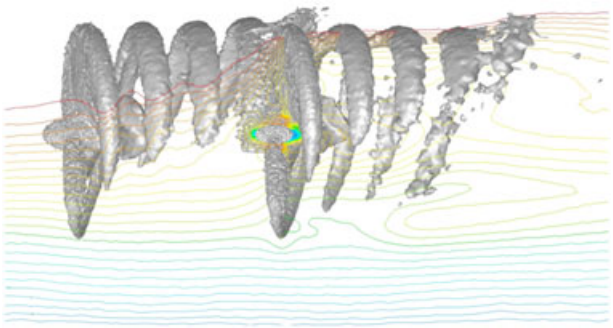

Figure 19. Iso-surfaces of constant vorticity. The centerline velocity profile is shown for the second rotor. Blades are in vertical position (0°).

for the two turbines are shown in Figures 21 and 22. The effect on the streamwise velocity from the upstream turbine is noticeable up to a distance of 8 radii downstream, at an azimuthal position of 0°. These velocity profiles compare well with wakes, measured and modeled, in the literature.[5,7,19] The source of the performance degradation of the downstream turbine (i.e. reduced lift coefficient) can be seen in Figure 21 at a distance of $x/R = 2$. The vertical velocity profile shows significant shear across almost the entire rotor disk, up to a height of $0.8R$ above the axis, because of the mixing induced by the upstream rotor on the velocity profile. This correlates well with the loss in lift experienced by the blade in the downstream turbine that crosses the wake at positions from 0° to 180°, as shown in Figure 14.

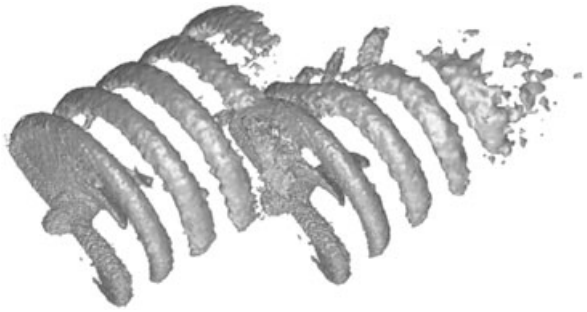

Figure 20. Iso-surfaces of constant vorticity shown with blades at 45° position.

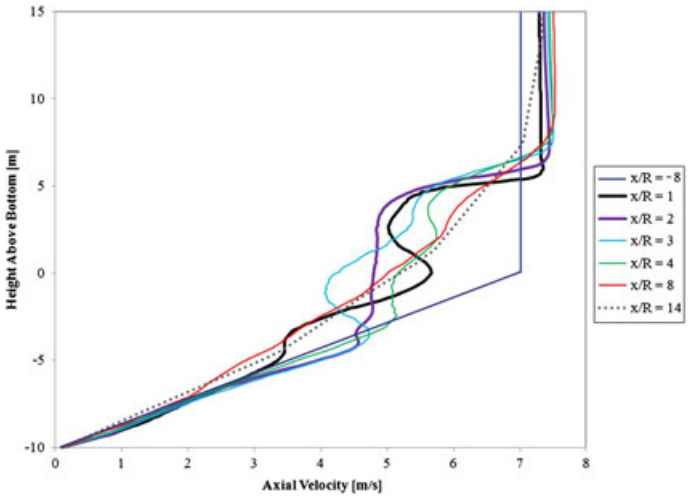

Figure 21. Centerline velocity profile for upstream rotor. x/R dimensions are given with respect to upstream rotor. The downstream rotor is located at $x/R = 2$.

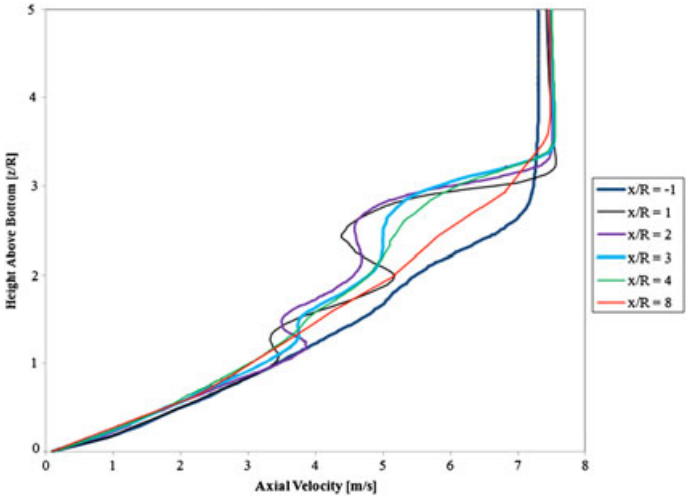

Figure 22. Centerline velocity profile for downstream rotor. x/R dimensions are given with respect to the downstream rotor. $x/R = -2$ would correspond to the location of the upstream rotor. Note the centerline plane for this turbine corresponds to the plane across the tip of the upstream turbine, so the profiles shown here do not correspond to any shown in Figure 21.

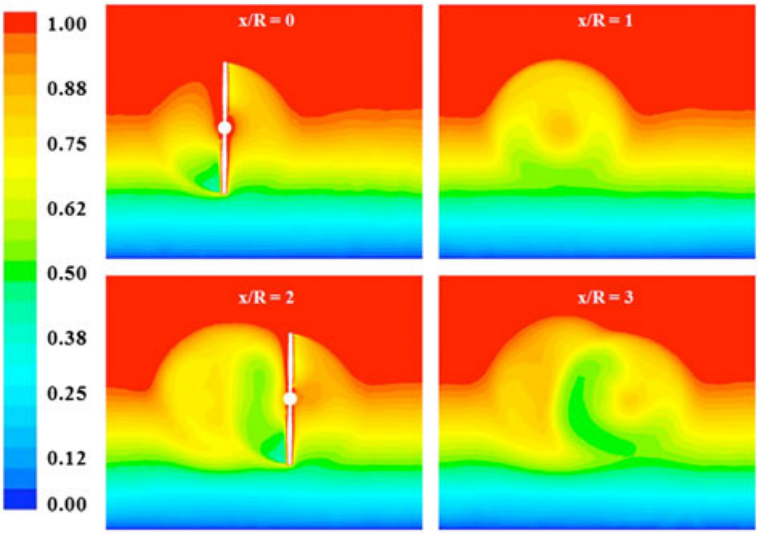

Figure 23. Velocity contours (non-dimensionalized with the free stream value of 7 m s^{-1}) at four different cross sections in the Y–Z plane. The view is from upstream, so that the blades are rotating counterclockwise.

The interaction between the wakes of the upstream turbine and the downstream turbine can be studied by taking cross sections of the flow field at different distances downstream. In Figure 23, we show four such cross sections, looking downwind so the turbines rotate counterclockwise, at the location of the two turbines ($x/R = 0$ and $x/R = 2$) and at locations just downstream of the first turbine ($x/R = 1$) and just downstream of the second turbine ($x/R = 3$). In this last subfigure, at $x/R = 3$, the downstream wake can be observed being drawn up and to the left. Notice the low momentum fluid in green, left behind by the second turbine after passing through the first turbine wake, moving up and spreading left in the counterclockwise motion of the wake from the upstream turbine. This interaction between wakes is similar to the results shown recently by Troldborg *et al.*[20]

5. CONCLUSIONS

The understanding of performance characteristics of rotors in shear flow is an important step to optimize rotor arrays in wind or tidal stream farms. We have used a fully 3D, time-accurate CFD simulation to improve on the current understanding of the effect of a shear freestream velocity profile, the wake of a previous turbine and the combination of the two effects, on overall turbine performance. These CFD simulations represent the highest fidelity representation of the turbine geometry and boundary conditions available to date, but still have some limitations in terms of the use of a turbulence model for closure and in the spatial discretization of the flow field. A sliding mesh numerical approach has been used for first time to model multiple rotors in a sheared inlet wind profile. We use an SST $\kappa - \omega$ turbulence model to capture the details of the wall bounded turbulence on the blades, as well as the free shear turbulence in the wake. Although other turbulence models can, and should, be tested in conjunction with this model, we found this to be satisfactory tool to perform a detailed flow analysis of wind turbines in a complex environment that closely reproduces the physics of actual application conditions, deviating from the typical uniform free stream flow. The lift and drag coefficients of the upstream rotor are in qualitative agreement with previous work performed on a single rotor in shear flow. These coefficients have a sinusoidal profile, with a phase shift that decreases for blade sections further from the hub. The lift and drag coefficients of the downstream rotor are strongly affected by the wake of the upstream rotor in this case of very aggressive spacing and demonstrate a noticeable degradation in performance. In the analysis of the lift and drag coefficients of the downstream turbine, we found a complex non-linear interaction with the shear inlet profile and the wake, with localized enhancement of the performance at 90° and 315° due to the symmetry-breaking combination of shear in the incoming velocity and rotation due to the upstream wake. Lateral spacing rules, therefore, need to take the direction of rotation and the operational tip speed ratio into account. Iso-surfaces of the vorticity illustrate the skewing of the wake due to the shear profile and the interaction of the downstream blade with the wake of the upstream rotor. 3D time-accurate CFD calculations are computationally expensive, but provide insight to the transient nature of the aerodynamic forces acting on the rotor blade. These updated aerodynamic forces can be used to improve the current BEM approach and provide a more realistic representation of the loading and simulated wake. These improved models can be applied in turbine array predictions, allowing the designer to optimize spacing and further reduce cost.

REFERENCES

1. Malcolm D, Hansen A. WindPACT turbine rotor design, specific rating study, 2003. National Renewable Energy Laboratory (NREL), Golden, CO.
2. Kelley ND, Jonkman BJ, Bialasiewicz JT, Scott GN, Redmond LS. Impact of coherent turbulence on wind turbine aeroelastic response and its simulation. In *Windpower 2005 Conference Proceedings (CD-ROM)*. American Wind Energy Association; Content Management Corp.: Denver, CO, Washington, DC, 2005; 22. NREL Report No. CP-500-40187.
3. Vermeer L, Sørensen J, Crespo A. Wind turbine wake aerodynamics. *Progress in aerospace sciences* 2003; **39**(6-7): 467–510.
4. Carcangiu. *CFD-RANS study of horizontal axis wind turbine*, PhD Thesis, Universita degli Studi di Cagliari, Italy, 2008.
5. Zahle F, Sørensen N, Johansen J. Rotor aerodynamics in atmospheric shear flow, *2008 European Wind Energy Conference and Exhibition*, Brussels, Belgium, March 31–April 3, 2008; 120–124.
6. Wußow S, Sitzki L, Hahm T. 3D-simulation of the turbulent wake behind a wind turbine. *Journal of Physics: Conference Series* 2007; **75**: 012–033. IOP Publishing.
7. Sørensen N, Johansen J. UPWIND, Aerodynamics and aero-elasticity rotor aerodynamics in atmospheric shear flow, *2007 European Wind Energy Conference and Exhibition*, Aalborg University, Denmark, 2007.
8. Pope S. *Turbulent flows*. Cambridge University Press: Cambridge, UK, 2000.
9. Menter F. Improved two-equation k-omega turbulence models for aerodynamic flows. *NASA STI/Recon Technical Report N* 1992; **93**(22): 809.
10. Barth T, Jespersen D. The design and application of upwind schemes on unstructured meshes, *AIAA, Aerospace Sciences Meeting, 27th*, Reno, NV. USA, Jan. 9-12, 1989.
11. Hand M, Simms D, Fingersh L, Jager D, Cotrell J. Unsteady Aerodynamics Experiment Phase V: Test Configuration and Available Data Campaigns, National Renewable Energy Laboratory, 2001.
12. Do T, Chen L, Tu J. Numerical study of the effect of trailing edge bluntness on highly turbulent hydrofoil flow. In *Proceedings of the 7th Biennial Engineering Mathematics and Applications Conference, EMAC-2005, ANZIAM J.*, Vol. 47, Stacey A, Blyth B, Shepherd J, Roberts AJ (eds), 2007. C822–C839 http://anziamj.austms.org.au/V47EMAC2005/Do[July 13, 2007].
13. Schreck S. Spectral content and spatial scales in unsteady rotationally augmented flow fields. *Journal of Physics: Conference Series* 2007; **75**: 012–024. IOP Publishing.
14. Zahle F, Sørensen N. On the influence of far-wake resolution on wind turbine flow simulations. *Journal of Physics: Conference Series* 2007; **75**: 012–042. IOP Publishing.
15. Auburn S, España G, Devinant P. Physical modelling of the far wake from wind turbines. Application to wind turbine interaction, *EWEC2007*, Milan, Italy, May 7, 2007.
16. Duque E, Burkland M, Johnson W. Navier–Stokes and comprehensive analysis performance predictions of the NREL phase VI experiment. *Journal of Solar Energy Engineering* 2003; **125**: 457–467.
17. Sørensen N, Michelsen J, Schreck S. Navier–Stokes predictions of the NREL phase VI rotor in the NASA Ames 80 ft × 120 ft wind tunnel. *Wind Energy* 2002; **5**(2-3): 151–169.
18. Salim S, Cheah S. Wall Y strategy for dealing with wall-bounded turbulent flows, *Proceedings of the International MultiConference of Engineers and Computer Scientists IMECS 2009*, Hong Kong, March 18-20, 2009; **2**: 2165–2170.
19. Cabezon D, Sanz J, Marti I, Crespo A. CFD modeling of the interaction between the surface boundary layer and rotor wake. Comparison of results obtained with different turbulence models and mesh strategies, *EWEC2009*, Marseille, France, March 16-19, 2009.
20. Troldborg N, Larsen G, Madsen H, Hansen K, Sørensen J, Mikkelsen R. Numerical simulations of wake interaction between two wind turbines at various conditions. *Wind Energy* 2011; **14**(7): 859–876. DOI: 10.1002/we433.